Active Flow Control over a Backward-Facing Step Using Plasma Actuation

R. Ruisi, H. Zare-Behtash,* and K. Kontis

School of Engineering, University of Glasgow, Scotland G12 8QQ, UK

R. Erfani

Manchester Metropolitan University,

School of Engineering, Manchester M1 5GD, UK

Abstract

Due to the more stringent aviation regulations on fuel consumption and noise reduction, the interest for smaller and mechanically less complex devices for flow separation control has increased. Plasma actuators are currently among the most studied typology of devices for active flow control purposes due to their small size and lightweight. In this study, a single dielectric barrier discharge (SDBD) actuator is used on a backward-facing step to assess its effects on the separated turbulent shear layer and its reattachment location. A range of actuating modulation frequencies, related to the natural frequencies of shear layer instability (flapping) and vortex shedding instability, are examined. The particle image velocimetry technique is used to analyse the flow over the step and the reattachment location. The bulk-flow experiments show negligible effects both on the shear layer and on the reattachment location for every frequency considered, and the actuator is not able to induce a sufficient velocity increase at the step separation point.

*Hossein.Zare-Behtash@glasgow.ac.uk

Nomenclature

AR	Aspect ratio	
ER	Expansion ratio	
c_f	Skin friction coefficient	
Δt	Time interval between two frames	[s]
δ,δ_{99}	Boundary layer thickness	[m]
δ^*	Displacement thickness	[m]
ϵ	Dielectric constant	
θ	Momentum thickness	[m]
f	frequency	[Hz]
h	Backward-Facing Step height	[m]
H	Shape factor for boundary layer	
Re	Reynolds number	
Re_h	Reynolds number (referred to the step height)	
Re_θ	Reynolds number (referred to the momentum thickness)	
ρ	Air density	$[\frac{kg}{m^3}]$
τ_w	Wall shear stress	$[\frac{kg}{ms^2}]$
τ_{xy}, Re_{xy}	Reynolds stress (xy plane)	$[\frac{kg}{ms^2}]$
St	Strouhal number	[-]
St_h	Strouhal number (referred to the step height)	
TI_u, TI_v	Turbulence intensity (for u and v velocity component)	
U, V, W	Mean velocities in the three directions	$[\frac{m}{s}]$
u, v, w	Instantaneous velocities in the three directions	$[\frac{m}{s}]$
V_{p-p}	Peak-to-peak voltage	[V]
X_R	Mean reattachment length	[m]

I. INTRODUCTION

A. Background

The interest for flow control has increased in the aerospace industry as higher performances are pursued and innovative approaches to drag reduction are introduced. Various methods for boundary layer control have been studied in the past decades in order to provoke or delay separation on airfoils[1] and turbine blades.[2] Kral[3] and Gad-El-Hak[4] published an extensive survey on this matter.

In the mid 1990's a new class of plasma actuators was introduced by Roth:[5] the dielectric barrier discharge (DBD) actuator. The single dielectric barrier discharge (SDBD) actuator, considered in this study, consists of two electrodes flush-mounted on opposite faces of a dielectric material, one exposed to the flow and the other placed under the body's surface. A high AC voltage, typically in the range 2 to 40 kV_{p-p}, is applied to the exposed electrode; Ramakumar[6] and Jolibois[7] showed that sine waveforms perform better in terms of plasma induced velocities. The high AC applied ionises the air adjacent to the exposed electrode creating plasma which, due to the electric field gradient, results in a body force inducing airflow along the actuator surface. Optimisation of such actuators are achieved by intervening on the temperature of the dielectric barrier, electrodes width, voltage, and modulation frequencies.[8–11]

Due to their fast flow response and the lack of moving parts, these actuators attracted much attention for flow control purposes.[12,13] The main disadvantage is the low induced velocities they produce, which currently limits its effectiveness to low Reynolds number applications, especially on small unmanned aircraft.[14,15] Nevertheless, DBD plasma actuators have shown their ability in boundary layer control,[16–21] manipulation of the laminar to turbulent transition point,[22,23] control separation on stationary[24] and oscillating airfoils[25] leading to reduced noise levels.[26]

Novel actuator designs have been developed to enhance flow authority by creating vortical structures to further energise the flow, a method which has been showed[27–29] to be more effective compared to the simple flow tripping effect given by momentum injection: promising results have been obtained with serpentine shaped actuators by Roy et al.[30,31]

B. Objective

Further research on the use of plasma actuators is needed in order to better understand its effectiveness and mechanism in promoting flow reattachment. Due to the lack of data on the effects of steady plasma actuation on the BFS test case for turbulent flows, the goal of this study is to investigate the effects of such actuators on the shear layer and its reattachment location. The actuator will be operated at different modulation frequencies to analyse the flow response, especially at the natural frequencies identified as fundamental to describe the flow instabilities.

C. The backward-facing step geometry

To assess the effectiveness of plasma actuators for flow control and the flow response to different modulation frequencies, the backward-facing step (BFS) geometry represents an interesting test case. The flow over a BFS, see Figure 1, is comprised of a separated shear layer from the edge of the step (i.e. separation point) and two main recirculation regions which form underneath the shear layer. Between the two, a second separation point occurs and its location ranges between $1.1h$ and $1.9h$ (where h is the step height).[32]

Far downstream, the reattachment location of the shear layer oscillates around a mean location due to the shear layer dynamic instability (generally referred to as the flapping effect), and its characteristic frequency, f, can be linked to the fluid velocity, U, and the step height, h, with a Strouhal number:

$$St_h = \frac{fh}{U} \tag{1}$$

for Reynolds numbers greater than $5{\times}10^4$, the reattachment location tends to a constant value, oscillating around a mean location at a distance of $6{\pm}2h$ from the step.[33]

According to Driver et al.[34] the fluctuation of the shear layer is caused by roll-up and pairing vortical effects occurring in the shear layer, temporarily influencing the recirculation bubbles and, in turn, the reattachment point. A Strohual number $St_h = 0.2$ (based on the step height) characterises the vortex shedding frequency in the shear layer (also in accordance with Simpson et al.[35]) while a lower Strouhal number $St_h \approx 0.06$[36] characterises the flapping motion of the shear layer.[32,37] Flapping seems not to affect shear stresses in

the mean reattachment point, as the Reynolds stress measurements do not show significant difference.

Adams and Johnston[33,38] linked the upstream boundary layer thickness (δ/h) directly to the pressure change downstream, noticing that the peak wall static pressure rise at the reattachment point decreased for increasing values of δ/h and the location of this peak moved further downstream. Consequent to pressure decrease, a drop in turbulent intensity and shear stress is expected in the reattachment region.

Spazzini et al.[32] studied the behaviour of wall shear stress downstream of the step, in order to investigate the origin of the low-frequency motion whose behaviour is caused by the flapping motion of the free shear layer, as generally accepted.[34,36,37,39] This behaviour was confirmed and normalised frequencies between $St_h = 0.05$ to 0.07 were identified as the flapping frequencies (also in agreement with Driver et al.[34]) It was also suggested that the cause of the flapping motion resides in the instability of the secondary separation point (and thus in the second recirculation bubble). Heenan and Morrison[40] were able to remove the flapping frequency using permeable walls downstream of the step, hence relating this instability to pressure disturbances and vorticity from the reattachment region.

II. EXPERIMENTAL SETUP

A. Wind tunnel and model

The experiments were performed in a suction type, open circuit, low speed wind tunnel with a test section 5.5m long and a cross section of 0.9m×0.9m. A step height of 65mm was chosen and the freestream velocity was set at 15 m/s, so that the boundary layer thickness at the step location equated the step height, thus providing $\delta/h = 1$. The Reynolds numbers, referred respectively to the upstream momentum thickness and the step height, resulted $Re_\theta = 6370$ and $Re_h = 64000$. The aspect ratio of the model, that is the ratio between its span and its height, was $AR = 12.3$ and the expansion ratio of the tunnel, that is the ratio between the tunnel area after the step and before the step, was $ER = 1.08$.

B. SDBD actuator

The SDBD actuator is flush-mounted on the model; the high voltage electrode (exposed to the flow) was 3mm wide and the encapsulated one 50mm wide, both of them made of copper foil 74μm thick. The trailing edge of the high voltage electrode was placed at $0.8h$ from the step and no stream-wise offset was used between the two electrodes. The dielectric barrier is made of Kapton tape, a polymide film with a low dielectric constant ($\epsilon \approx 3.4$). Kapton tape was layered between the two electrodes with a total thickness of 540μm. Particular care was put in the layering of the tape in order to avoid bubbles, and confidence in the reliability of such material was given by successful previous studies.[8]

The SDBD actuator setup is presented in Figure 2. The electric apparatus used to supply the plasma actuator is identical to that used by Erfani et al.[41,42] The experiments with the plasma actuator were performed at 14kV$_{p-p}$ and $10KHz$ driving frequency. The output current waveform is shown in Figure 3.

The SDBD actuator was tested at modulation frequencies 15, 50, 100, 250 and 450 Hz which correspond to Strouhal numbers $St_h = 0.065$, 0.2, 0.41, 1.08 and 1.95, respectively. This large range is necessary to assess actuator's effects on both the flapping motion ($St_h = 0.06$) and vortex shedding instability ($St_h = 0.2$), as well as to check the response to higher harmonics.

C. Particle image velocimetry (PIV)

A PIV system identical to Ukai et al.[43] was used to obtain quantitative information of the flow. Olive oil particles, with a diameter in the order of 1μm,[44] were used as seeders. The PIV system used for the experiments was a *Litron Lasers - Nano L PIV*, double oscillator laser system, providing a 532nm Nd:YAG pulsed laser beam. A *Lavision ImagerProX 2M* (1600×1200 pixel resolution, 7.4μm pixel size) was used to capture the raw images for processing. The time interval between the two PIV frames was optimised by the PIV software for each case based on the field of view and the flow velocity. The recorded image pairs were initially divided into 32×32 pixel interrogation windows and processed with a cross correlation algorithm; the interrogation windows were then refined to 16×16 pixel squares.

D. Constant temperature hot wire anemometry

A 2-component DANTEC constant temperature hot wire anemometry (CTA) system was used to measure the stream-wise and transverse velocity components. The wires are made of tungsten, $5\mu m$ in diameter and $1.5mm$ in length. The temperature of the hot-wire sensor is controlled by a CTA electronic board. An ADC card with a maximum data-sampling rate of $100KHz$ with a resolution of 12 bit is used for digitising the analogue signals transmitted by the sensor. The frequency response (based on square-wave test) of CTA and selected probe showed that the maximum sampling rate could be approximately $95kHz$. The sampling rate is set to $5kHz$ for 4 seconds of recording and the filtering cut-off frequency of $2kHz$ is used for the measurement purposes, which is adequate for the acquisition of turbulent flows. The probe is traversed in a vertical plane, passing through the centreline of the test section. A digital gage is positioned on the traverse to measure the height from the wall accurately ($\pm$ $0.005mm$). The hot wire probe was calibrated within air velocities ranged between 0 and 16 m/s and pitch angles from -30 to 30 degrees.

To ascertain the within the CTA measurement technique, five sample runs were conducted at the centreline ($x = -h$, $z = 0$) and velocity measurements were taken in order to compute the standard deviation amongst the respective values. The average between all standard deviations acts as the uncertainty; the value is found to be $\pm$0.092 m/s.

III. RESULTS

Hot-wire anemometry at different stream-wise locations, in Figure 4(a), shows boundary layer thickness $\delta_{99} = 65$mm, displacement thickness $\delta^* = 8.2$mm and momentum thickness $\theta = 5.9$mm, giving a shape factor $H = \delta/\theta = 1.4$, proving a nearly fully developed turbulent boundary layer. The two-dimensionality of the flow (guaranteed for $AR > 10$[45]) was validated by plotting span-wise velocity profiles for fixed $x = -h$, in Figure 4(b). Turbulence intensity levels TI_u and TI_v exhibit values respectively lower than 10% and 5% before the step in Figure 5. Once the downstream reattachment length was determined at about $6h$ using oilflow, a pressure tapping was used to capture the pressure fluctuations. A pressure transducer was flush-mounted to the tunnel floor, downstream of the step and used at two different sampling frequencies (1kHz and 500Hz). Spectral density of pressure in Figure 6

shows a peak with a Strouhal number $St_h = 0.06$, correspondent to the shear layer flapping frequency in agreement with literature. A second peak is obtained for St_h =0.12 which can be linked to vortex instability.

Due to the turbulent and unsteady nature of the flows studied in the experiments, it is important to increase the number of recorded data in order to reduce the uncertainties and deal with velocity values which are statistically correct. PIV is an instantaneous measurement technique and, in order to deal with statistically correct data, ensemble-average of big number of vector maps (or vector fields) becomes necessary, in order to calculate the spatial distribution of turbulent properties over the measurement plane:

$$U_{i,j} = \frac{1}{N} \sum u_{i,j} \tag{2}$$

where N is the number of vector fields recorded, u is the instantaneous value and U is the averaged value. Thus, in order to assess the statistical accuracy of the measurements, velocity values were compared for ensembles of 10, 20, 50 and 200 vector maps, randomly selected from a 1000 vector fields ensemble recorded at the step location, as suggested by Uzol and Camci[46] and Ullum et al.[47] Six random locations in the field of view, indicated in Figure 7, were selected as samples and their stream-wise velocity component compared. As evident in Figure 8 and mean of the velocity, standard deviation and standard error provided in Table I, the obtained velocities tend to converge for ensembles with a number of vector fields larger than 200 and the standard error of the ensembles decreases substantially as the number of vector fields increases, with exception of sample points $P1$ and $P4$ which exhibit higher error since located into the shear layer region, hence influenced by the high instability of the flow. It is thus possible to state that a good accuracy can be achieved with a number of vector fields equal or greater than 200. Moreover, in order to guarantee the quality of the collected data, only vectors with a Q-factor greater than 1.7 have been retained (this parameter is used to assess the quality of the cross-correlation process, defined as $(P1 - m)/(P2 - m)$, where $P1$ and $P2$ are the two highest signal peaks, while m is the average background noise). The number of retained vectors, for every image pair considered, was equal or greater than 70%.

A. SDBD actuator characteristics in quiescent flow

Initially, the actuator's performance was studied in quiescent flow. For each modulation frequency 250 vector fields were recorded with a time interval between the two PIV frames of $\Delta t = 450\mu$s. Contours of the average stream-wise velocity component are shown in Figure 9(a) for the 15Hz modulation frequency case. In Figure 9(b), a velocity peak of 1.41m/s is visible in the shear layer approximately at $x/h = 0.15$ and $y/h = 1.05$ (or $0.95h$ from the exposed electrode). The highest velocity was reached for the 450Hz case, although a similar behaviour was exhibited for all the other cases. From the velocity profiles in Figure 10 it is clear that, upstream of the step, the velocity increases with increasing actuating frequency (Figure 10(a)): the induced velocity at 450Hz peaks as much as twice the velocity for the 15Hz case. Downstream of the step, instead, the profiles show no dependence on the frequency.

B. BFS Baseline

Contours of the average stream-wise velocity component are shown in Figure 11(a) for the baseline case, that is without feeding the actuator. For every modulation frequency, 1000 vector fields (5 repeats of 200 image pairs) were recorded, using $\Delta t = 31\mu$s. The secondary recirculation region at the bottom of the step spans approximately $0.5h$ vertically, while its horizontal reattachment point lies outside of the current field of view. The comparison, for every frequency, of the secondary vortex bubble sizes and their secondary reattachment location beneath the step, showed no significant change, suggesting no influence of the actuator on the behaviour of the separated shear layer.

Profiles of the stream-wise velocities are plotted along the x-direction in Figure 11(b), again for $y/h = 1.05$: all the profiles follow a similar trend and the highest peak, $0.705u/U$ is reached by the 450Hz plot slightly after the step, corresponding to $\sim$4% increase compared to the baseline. An average velocity increase of $0.03u/U$ is found further away from the step. Additionally, the velocity profiles taken at five different locations downstream of the step edge are plotted in Figure 12 for the baseline and 15Hz only: identical profiles are exhibited for the other frequency cases, showing that shear layer is not affected by any actuating frequency. Therefore, it can be stated that, for such flow conditions, the steadily-excited

SDBD actuator is ineffective for each actuating frequency considered.

C. Reattachment location

Contours of the average stream-wise velocity component for the reattachment region are shown in Figure 13 for the baseline case. The end of the primary recirculation bubble is visible at approximately $5.5h$. Velocity profiles, compared for each modulation frequency, are shown in Figure 14 close to the reattachment point ($x/h = 6.0$) and far from it ($x/h = 6.8$), exhibiting identical behaviours for all the actuating frequencies.

The Reynolds stress, τ_{xy}, is responsible for momentum transfer due to turbulent fluctuations and is an indicator of the vorticity and rms velocities, hence being an important parameter to assess the promotion of the shear layer reattachment.[27,48] Contours of Reynolds stress for the baseline are shown in Figure 15(a). The highest levels of stress are found in correspondence of the region with the highest turbulence (visible in blue), due to the effects of the impinging shear layer and recirculation bubble reattachment. When compared to the baseline results, no remarkable differences are visible along the stream-wise direction, as the profiles in Figure 15(b,c,d) show. The plots of Reynolds stress for the 15Hz case, corresponding to $St_h = 0.06$, i.e., the flapping frequency, show higher values for the three considered locations closest to the estimated reattachment point, with an average increase of 15 to 20% compared to the other plots. However, a clear conclusion cannot be drawn due to the irregular behaviour of the plots.

The reattachment location (as any stagnation point), X_R, can be defined as the locus where the friction coefficient c_f is zero, due to the absence of a velocity gradient at the wall. Moreover, the reattachment point will have a 50% probability of stream-wise velocity component going forward or backward, due to its stagnant nature.[32,49–51] Figure 16(a) shows the flow streamlines superimposed on the contours of friction coefficient: a mark indicates the reattachment region, where the friction coefficient at the wall shows quasi-zero values and the streamlines reattach on the surface. Figure 16(b) shows the stream-wise component of velocity at different heights. The plots from $y/h = 0.02$ to 0.04 have a similar behaviour, and the velocity component reaches zero for $x/h \approx 5.75$, in the baseline case (values for $y/h = 0.01$ are, instead, influenced by surface errors). The estimated reattachment locations for every frequency case are summarised in Table II: the reattachment point exhibits a

maximum drift of ∼3%, thus not justifying any effectiveness of the actuator.

It is clear from these data that the SDBD actuator has no remarkable influence on the reattachment location and the lack of any effect on the Reynold stress can be interpreted as its ineffectiveness to enhance the formation of vortical structures in the shear layer, hence not promoting reattachment.

IV. CONCLUSIONS

The effects of an SDBD plasma actuator have been examined on the flow over a backward-facing step with a step height of 65mm and $\delta/h = 1$. Experiments have been performed in a subsonic wind tunnel and PIV technique was used to assess the flow response to the actuator, once a good statistical convergence was achieved.

When tested in quiescent-flow, the actuator showed an induced-velocity peak of 1.41m/s at $x = 0.15$h. Only a small velocity increase was obtained for the bulk-flow case, with a peak of ∼4% compared to the baseline. The different actuating frequencies showed no remarkable effects on the velocity profiles downstream of the actuator or in the recirculation bubbles. The reattachment point was estimated looking both at the friction coefficient and the velocity streamlines close to the floor surface, showing to be unaffected by the different modulation frequencies considered. Reynolds stress shows only slight variations, not linkable to any frequency-related influence on the shear layer.

It can be concluded that, for a turbulent regime, the steadily-excited SDBD actuator has no flow authority, thus not promoting the shear layer reattachment. Reasons for this ineffectiveness are attributed to the mechanism of interaction between the mean flow and the induced flow, limited to simple flow tripping. As already suggested, the Reynolds stress has great importance in the promotion of mixing, hence being fundamental in momentum transfer and, in turns, to the promotion of reattachment. Span-wise vortical structures, caused by unsteady actuation or 3-dimensional effects induced by the side walls, have shown greater effectiveness on the reattachment promotion, due to the different mechanism of interaction with the flow.

It is strongly suggested to further investigate unsteady actuation using a duty cycle pattern (which also decreases power consumption), focusing on the natural frequencies of shear layer instability and vortex shedding instability, as well as new electrode designs, such

as serpentine-shaped actuators, which proved enhanced flow authority due to formation of vortical structures, promoting mixing and flow reattachment.

V. ACKNOWLEDGMENTS

The authors are grateful for the technical help and support of Dr. K.H. Lo, and the useful discussions of Prof. S. Roy. This work was supported by the 7th Framework Program FP7/2010-2013 MARS (grant agreement number 266326).

[1] Post, M.L., Corke, T.C., "Separation control on high angle of attack airfoil using plasma actuators," *AIAA Journal* **42**, 2177–2184, (2004).

[2] Huang, J., Corke, T.C., Thomas, F.O., "Plasma actuators for separation control of low-pressure turbine blades," *AIAA Journal* **44**, 51–57, (2006).

[3] Kral, L.D., "Active flow control technology," *ASME Fluids Engineering Technical Brief*, (2000).

[4] Gad-El-Hak, M., "Flow Control: Passive, Active, and Reactive Flow Management," *Cambridge University Press*, (2000).

[5] Roth, J.R., "Industrial Plasma Engineering," *CRC Press*, (1995).

[6] Ramakumar, K., Jacob, J.D., "Flow control and lift enhancement using plasma actuators," *35th Fluid Dynamics Conference*, Toronto, (2005).

[7] Jolibois, J., Moreau, E., "Enhancement of the electromechanical performances of a single dielectric barrier discharge actuator," *IEEE Transactions on Dielectrics and Electrical Insulation* **16**, 758–767, (2009).

[8] Erfani, R., Zare-Behtash, H., Kontis, K., "Plasma actuator: Influence of dielectric surface temperature," *Experimental Thermal and Fluid Science* **42**, 258–264, (2012).

[9] Corke, T.C., Post, M.L., Orlov, D.M., "Single dielectric barrier discharge plasma enhanced aerodynamics: Physics, modeling and applications," *Experiments in Fluids* **46**, 1–26, (2009).

[10] Geuns, R., Goekce, S., Plyushchev, G., Leyland, P., Pimentel, R., deChamplain, A., Jean, Y., "Understanding SDBD Actuators: An Experimental Study on Plasma Characteristics," *45th AIAA Plasmadynamics and Lasers Conference*, 2014-2811, (2014).

[11] Moreau, E., "Airflow control by non-thermal plasma actuators," *Journal of Physics D: Applied Physics* **40**, 605–636, (2007).

[12] Balcon, N., Benard, N., Moreau, E., "Formation process of the electric wind produced by a plasma actuator," *IEEE Transactions on Dielectrics and Electrical Insulation* **16**, 463–469, (2009).

[13] Erfani, R., Erfani, T., Utyuzhnikov, S.V., Kontis, K., "Optimisation of multiple encapsulated electrode plasma actuator," *Aerospace Science and Technology* **26**, 120–127, (2013).

[14] Patel, M.P., Ng, T.T., Vasudevan, S., Corke, T.C., He, C., "Plasma actuators for hingeless aerodynamic control of an unmanned air vehicle," *Journal of Aircraft* **44**, 1264–1274, (2007).

[15] Goksel, B., Greenblatt, D., Rechenberg, I., Bannasch, R., Paschereit, C.O., "Plasma flow control at MAV Reynolds numbers," *3rd US-European Competition and Workshop on Micro Air Vehicle Systems and European Micro Air Vehicle Conference and Flight Competition*, (2007).

[16] Porter, C.O., McLaughlin, T.E., Enloe, C.L. Font, G.I., Roney, J., Baughn, J.W., "Boundary layer control using a DBD plasma actuator," *45th AIAA Aerospace Sciences Meeting and Exhibit*, Reno, AIAA-2007-786, (2007).

[17] Opaits, D.F., Roupassov, D.V., Starikovskaia, S.M., Starikovskii, A.Y., Zavialov, I.N., Saddoughi, S.G., "Plasma control of boundary layer using low-temperature non-equilibrium plasma of gas discharge," *43rd AIAA Aerospace Sciences Meeting and Exhibit*, Reno, AIAA-2005-1180, (2005).

[18] Boxx, I.G., Rivir, R.B., Newcamp, J.M., Woods, N.M., "Reattachment of a separated boundary layer on a flat plate in a highly adverse pressure gradient using a plasma actuator," *3rd AIAA Flow Control Conference*, San Francisco, AIAA-2006-3023, (2006).

[19] Jacob, J., Rivir, R.B., Carter, C., Estevadeordal, J., "Boundary layer flow control using ac discharge plasma actuators," *AIAA 2nd Flow Control Meeting*, Portland, AIAA-2004-2128, (2004).

[20] Font, G.I., "Boundary layer control with atmospheric plasma discharges," *AIAA Journal* **44**, 1572–1578, (2006).

[21] Hale, C., Erfani, R., Kontis, K., "Multiple encapsulated electrode plasma actuators to influence the induced velocity: Further configurations," *40th Fluid Dynamics Conference and Exhibit*, Chicago, AIAA-2010-5106, (2010).

[22] Grundmann, S., Tropea, C., "Delay of boundary-layer transition using plasma actuators," *46th AIAA Aerospace Sciences Meeting and Exhibit*, Reno, AIAA-2008-1369, (2008).

[23] Peschke, P., Goekce, S., Leyland, P., Hollenstein, C. and Ott, P., "Experimental Investigation of Pulsed Dielectric Barrier Discharge Actuators in Sub- and Transonic Flow," *44th AIAA Plasmadynamics and Lasers Conference*, 2013-2885, (2013).

[24] He, C., Patel, M.P., Corke, T.C., "Plasma flaps and slats: an application of weakly ionized plasma actuators," *Journal of Aircraft* **46**, 864–873, (2009).

[25] Post, M.L., Corke, T.C., "Separation control using plasma actuators: dynamic stall vortex control on oscillating airfoil," *AIAA Journal* **44**, 3125–3135, (2006).

[26] Thomas, F.O., Kozlov, A., Corke, T.C., "Plasma actuators for cylinder flow control and noise

reduction," *AIAA Journal* **46**, 1921–1931, (2008).

[27] Huang, J., Corke, T.C., Thomas, F.O., "Unsteady Plasma Actuators for Separation Control of Low-Pressure Turbine Blades," *AIAA Journal* **44**, 1477–1515, (2006).

[28] Sun, M., Yang, B., Li, J.M., Lei, M.K., "Experimental investigation on stall separation control on NACA0015 airfoil by steady plasma aerodynamic actuation," *Advanced Materials Research* **516-517**, 726–730, (2012).

[29] Benard, N., Jolibois, J., Moreau, E., "Lift and drag performances of an axisymmetric airfoil controlled by plasma actuator," *Journal of Electrostatics* **67**, 133–139, (2009).

[30] Durscher, R.J., Roy, S., "Induced flow from serpentine plasma actuators acting in quiescent air," *49th AIAA Aerospace Sciences Meeting including the New Horizons Forum and Aerospace Exposition*, Orlando, AIAA-2011-957, (2011).

[31] Wang, C.C., Durscher, R.J., Roy, S., "Three-dimensional effects of curved plasma actuators in quiescent air," *Journal of Applied Physics* **109**, 083305, (2011).

[32] Spazzini, P.G., Iuso, G., Onorato, M., Zurlo, N., Di Cicca, G.M., "Unsteady behavior of back-facing step flow," *Experiments in Fluids* **30**, 551–561, (2001).

[33] Adams, E.W., Johnston, J.P., "Effects of the separating shear layer on the reattachment flow structure Part 2: Reattachment length and wall shear stress," *Experiments in Fluids* **6**, 493–499, (1988).

[34] Driver, D.M., Seegmiller, H.L., Marvin, J.G., "Time-dependent behavior of a reattaching shear layer," *AIAA Journal* **25**, 914–919, (1987).

[35] Simpson, R.L., Strickland, J.H., Barr, P.W., "Features of a separating turbulent boundary layer in the vicinity of separation," *Journal of Fluid Mechanics* **79**, 553–594, (1977).

[36] Simpson, R.L., "Aspects of turbulent boundary-layer separation," *Progress in Aerospace Sciences* **32**, 457–521, (1996).

[37] Eaton, J., Johnston, J., "Low frequency unsteadiness of a reattaching turbulent shear layer," *Turbulent Shear Flows 3*, 162–170, (1982).

[38] Adams, E.W., Johnston, J.P., "Effects of the separating shear layer on the reattachment flow structure Part 1: Pressure and turbulence quantities," *Experiments in Fluids* **6**, 400–408, (1988).

[39] Lee, I., Sung, H.J., "Characteristics of wall pressure fluctuations in separated and reattaching flows over a backward-facing step: Part I. Time-mean statistics and cross-spectral analyses," *Experiments in Fluids* **30**, 262–272, (2001).

[40] Heenan, A.F., Morrison, J.F., "Passive control of pressure fluctuations generated by separate flow," *AIAA Journal* **36**, 1014–1022, (2004).

[41] Erfani, R., Zare-Behtash, H., Kontis, K., "Influence of shock wave propagation on dielectric barrier discharge plasma actuator performance," *Journal of Physics D: Applied Physics* **45**, 225201, (2012).

[42] Erfani, R., Zare-Behtash, H., Hale, C., Kontis, K., "Development of DBD plasma actuators: The double encapsulated electrode," *Acta Astronautica* **109**, 132–143, (2015).

[43] Ukai, T., Zare-Behtash, H., Erdem, E., Lo, K.H., Kontis, K., Obayashi, S., "Effectiveness of jet location on mixing characteristics inside a cavity in supersonic flow," *Experimental Thermal and Fluid Science* **52**, 59–67, (2014).

[44] Ukai, T., Zare-Behtash, H., Lo, K.H., Kontis, K., Obayashi, S., "Effects of dual jets distance on mixing characteristics and flow path within a cavity in supersonic crossflow," *International Journal of Heat and Fluid Flow* **50**, 254–262, (2014).

[45] Brederode, V., Bradshaw, P., "Influence of the side walls on the turbulent center-plane boundary-layer in a square duct," *Journal of Fluids Engineering* **100**, 91–96, (1978).

[46] Uzol, O., Camci, C., "The effect of sample size, turbulence intensity and velocity field on the experimental accuracy of ensemble averaged PIV measurements," *4th International Symposium on Particle Image Velocimetry*, Göttingen, (2001).

[47] Ullum, U., Schmidt, J., Larsen, P.S., McCluskey, D.R., "Statistical Analysis and Accuracy of PIV Data," *Journal of Visualization* **1**, 205–216, (1998).

[48] Yoshioka, S., Obi, S., Masuda, S., "Organized vortex motion in periodically perturbed turbulent separated flow over a backward-facing step," *International Journal of Heat and Fluid Flow* **22**, 301–307, (2001).

[49] Westphal, R.V., Johnston, J.P., "Effect of initial conditions on turbulent reattachment downstream of a backward-facing step," *AIAA Journal* **22**, 1727–1732, (1984).

[50] Ra, S.H., Chang, P.K., Park, S.O., "Measurement of the forward-flow fraction using a split film sensor," *Experiments in Fluids* **10**, 57–59, (1990).

[51] Kasagi, N., Matsunaga, A., "Three-dimensional particle-tracking velocimetry measurement of turbulence statistics and energy budget in a backward-facing step flow," *International Journal of Heat and Fluid Flow* **16**, 477–485, (1995).

List of Figures

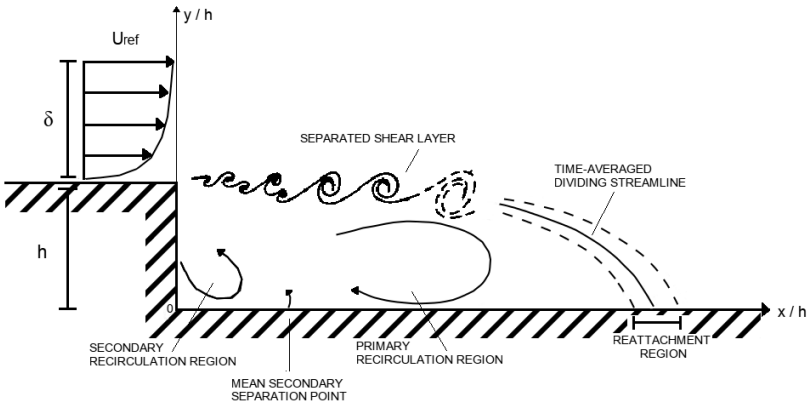

FIG. 1: Sketch of the flow characteristics over a backward-facing step.

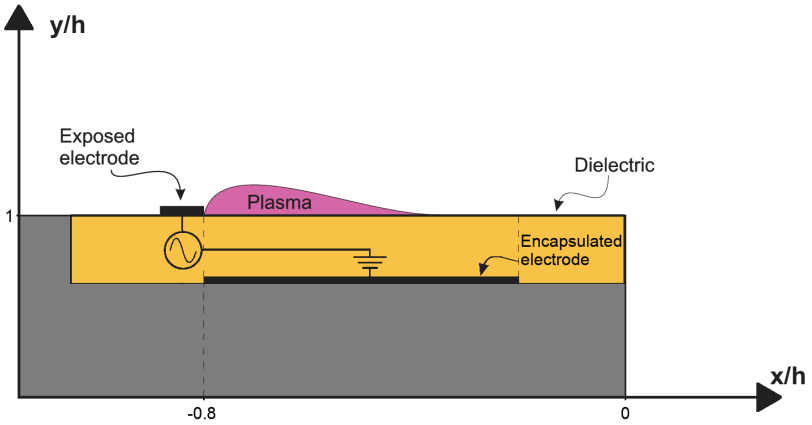

FIG. 2: Sketch of the SDBD actuator setup used (actuator not to scale).

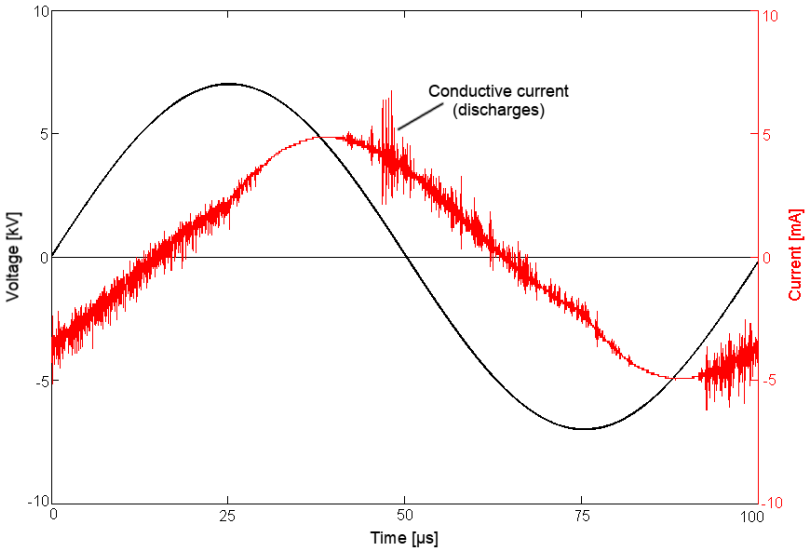

FIG. 3: Current and Voltage trace. Notice the plasma discharge.

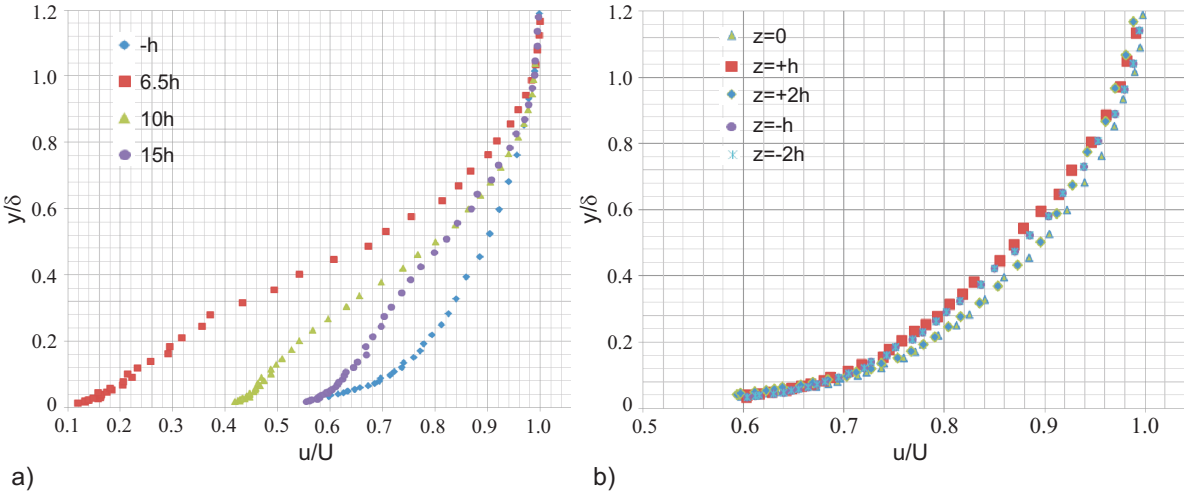

FIG. 4: Velocity profiles at: (a) different stream-wise, and (b) span-wise (x = -h) locations.

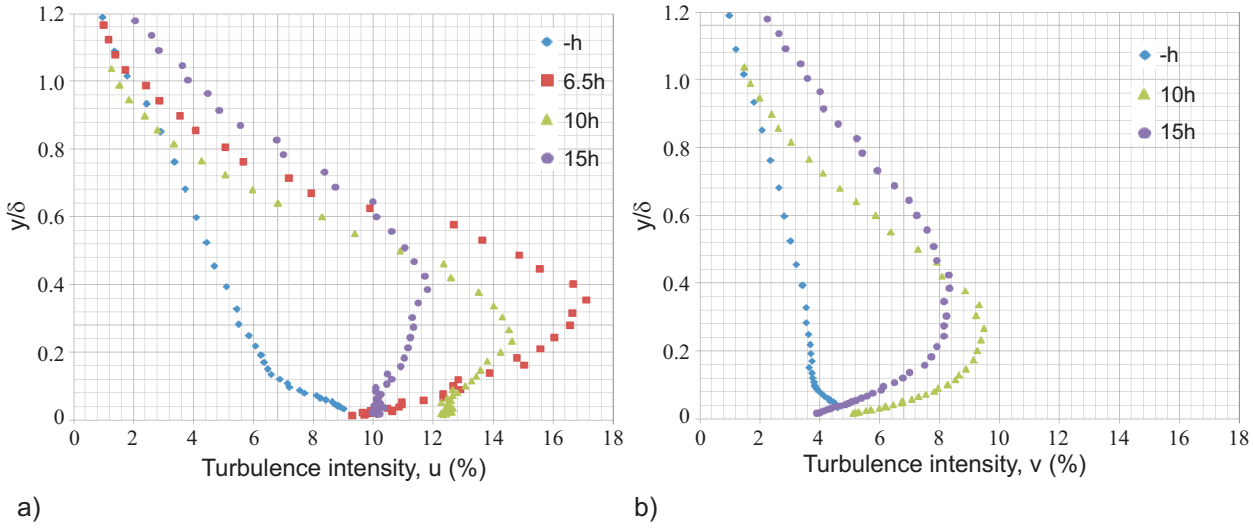

FIG. 5: Turbulence intensity profiles at different stream-wise locations along the centreline: (a) stream-wise component, and (b) vertical component.

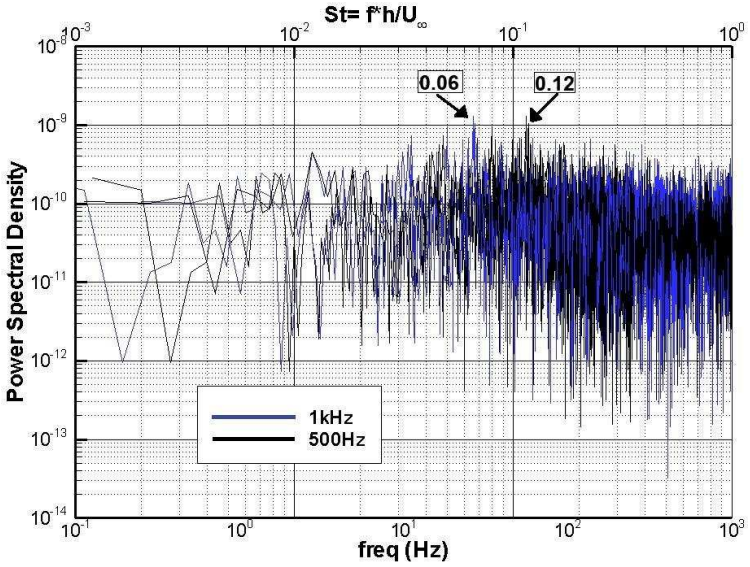

FIG. 6: Power Spectral Density from the pressure transducer, flush-mounted to the tunnel floor, showing peaks for $St_h = 0.06$ and $St_h = 0.12$.

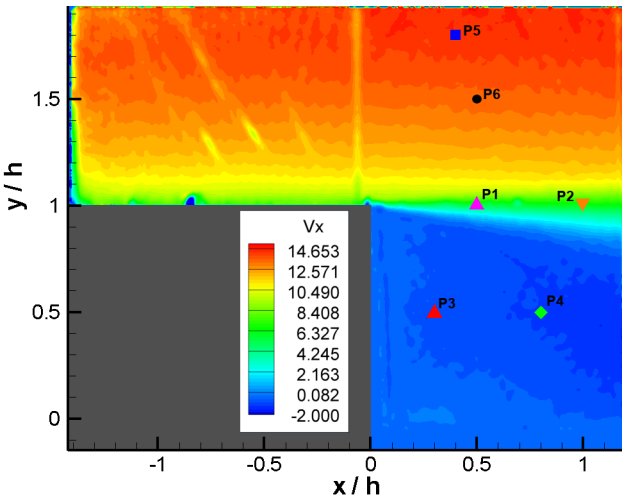

FIG. 7: Statistical analysis: map of the selected sampling points.

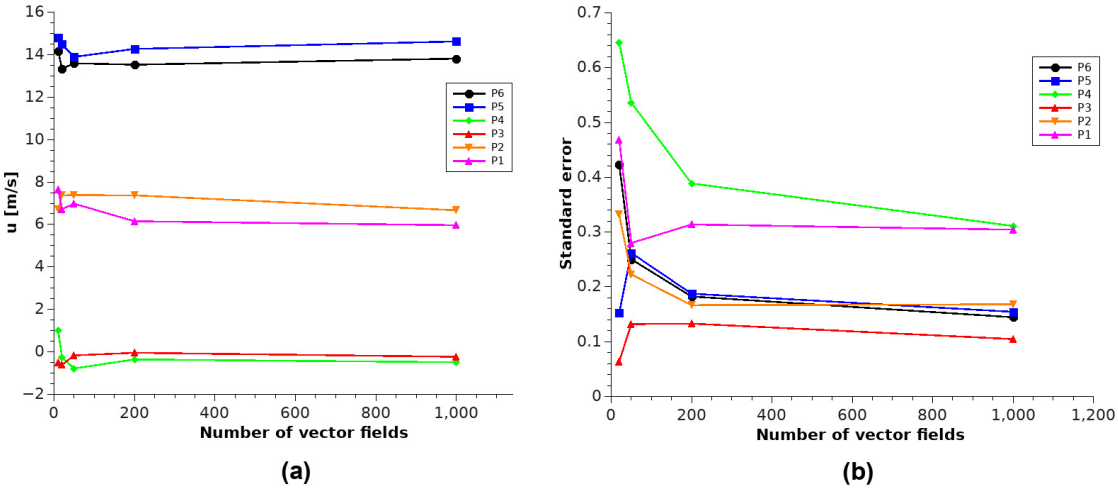

FIG. 8: Statistical analysis: (a) convergence of velocity for increasing number of vector fields; (b) standard error decreases for increasing number of vector fields.

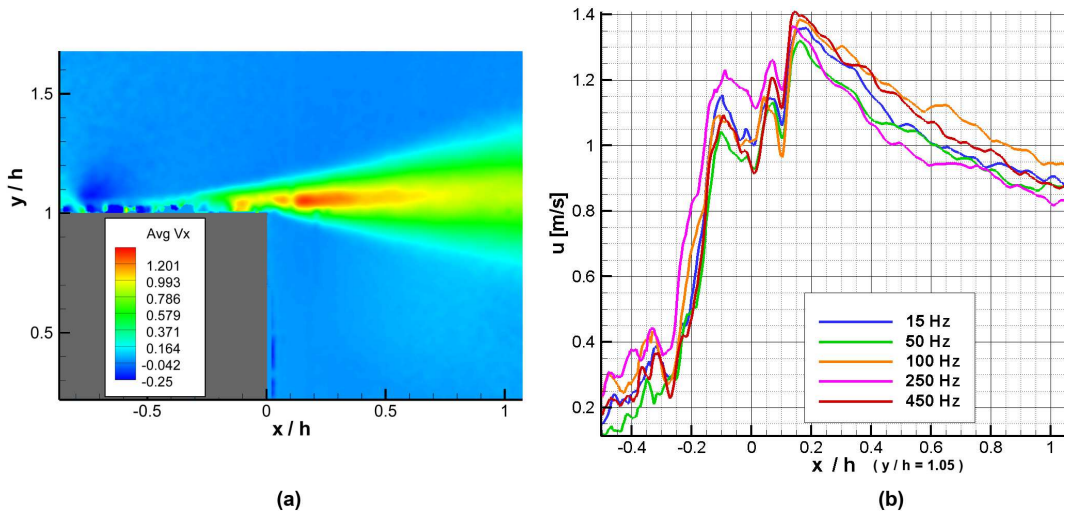

FIG. 9: No-flow case: (a) time-averaged u velocity component for the $15Hz$ case; (b) induced velocity profile along the stream-wise direction (at $y/h = 1.05$).

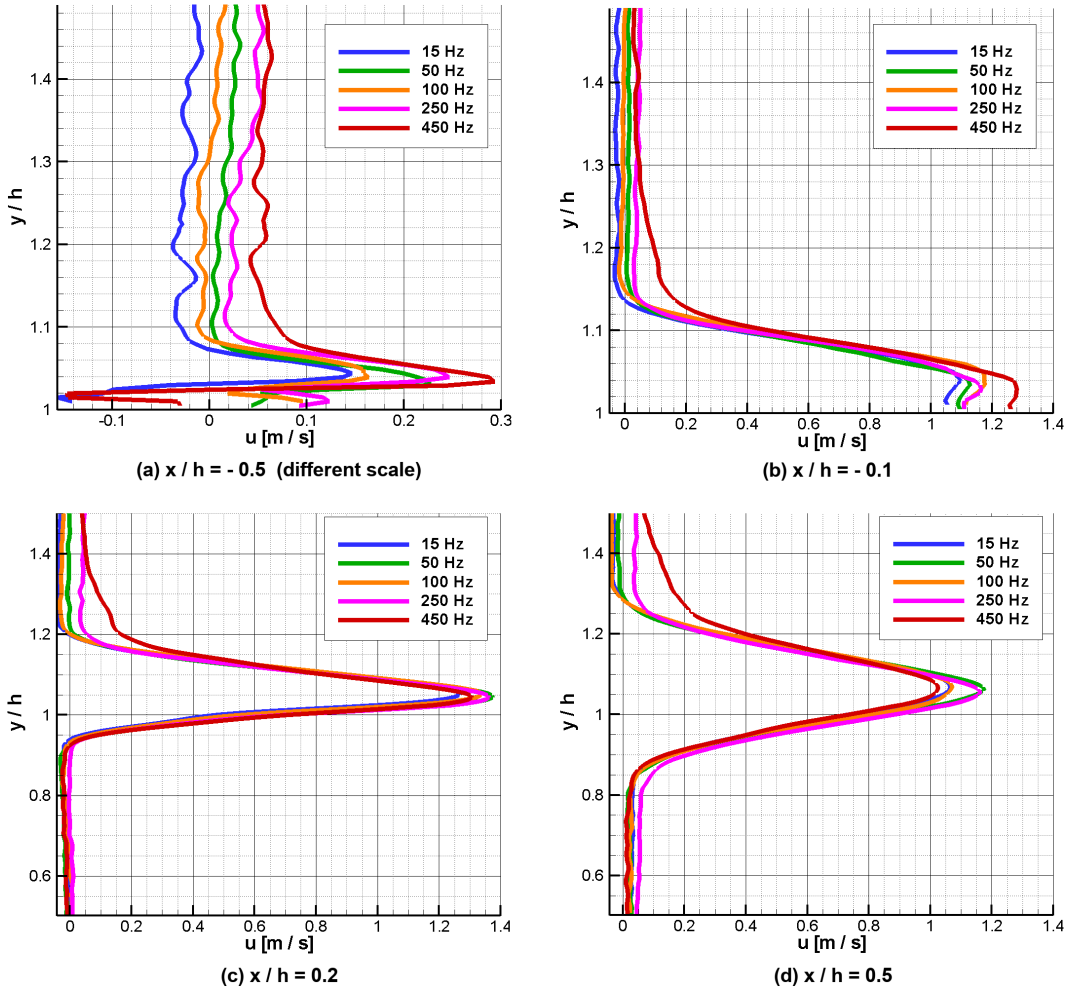

FIG. 10: No-flow case: effect of different frequencies on u profiles at various x/h locations.

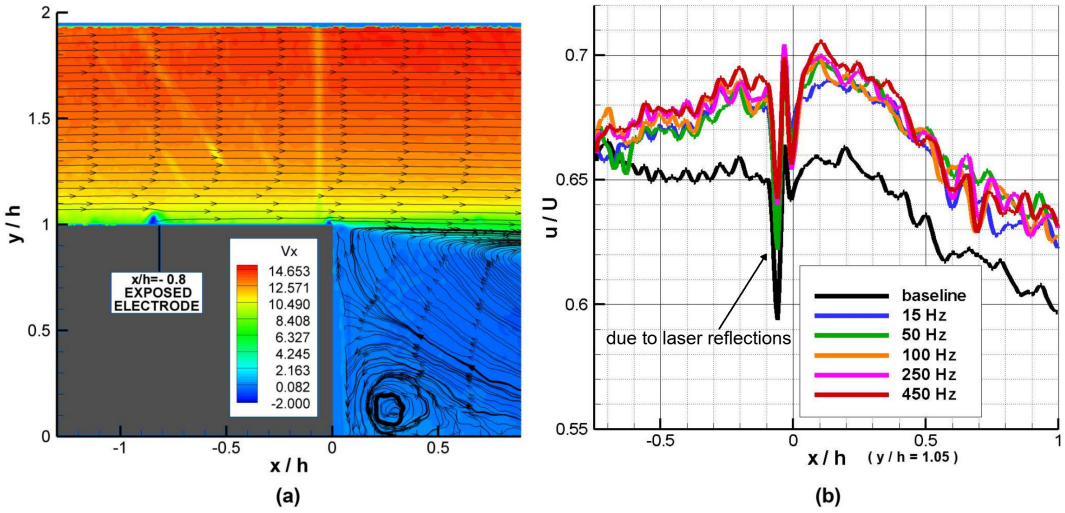

FIG. 11: (a) Time-averaged u velocity component (baseline). (b) Induced velocity profile along the stream-wise direction, at $y/h = 1.05$ (the visible discontinuity before the step edge is caused by laser reflections, visible in (a)).

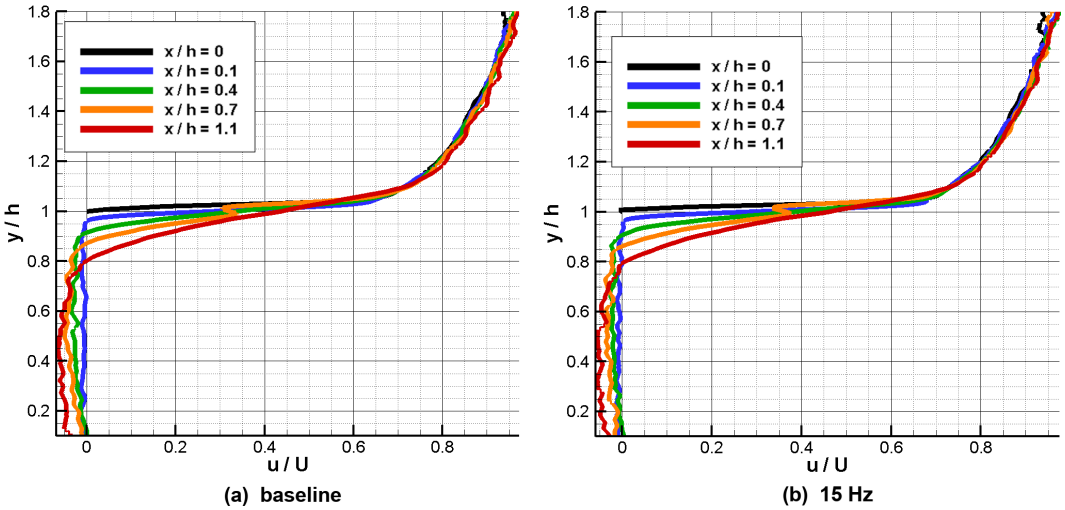

FIG. 12: Comparison of u profiles at different locations, for (a) baseline and (b) $15Hz$ case.

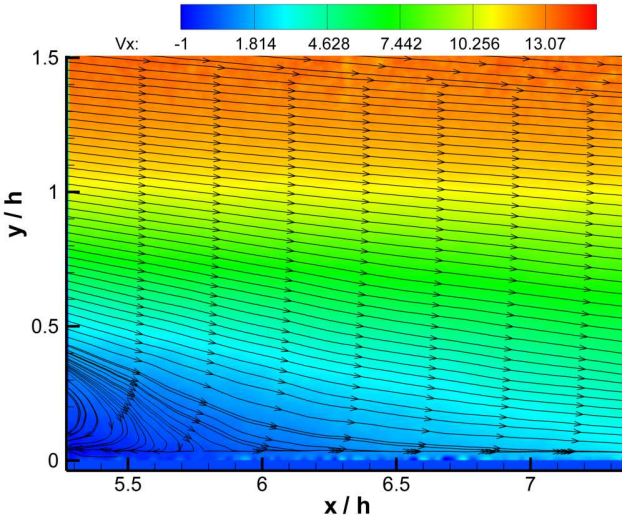

FIG. 13: Reattachment location: time-averaged u velocity component and streamlines, for the baseline case.

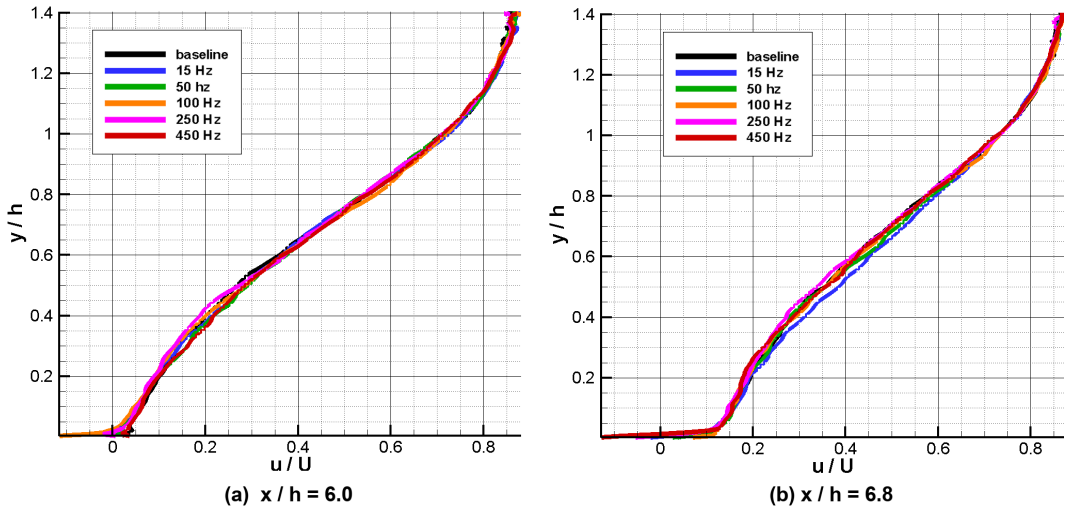

FIG. 14: Reattachment location: effect of different frequencies on u profiles at two specific locations: (a) $x/h = 6.0$, close to the reattachment point, (b) $x/h = 6.8$, downstream of the reattachment point.

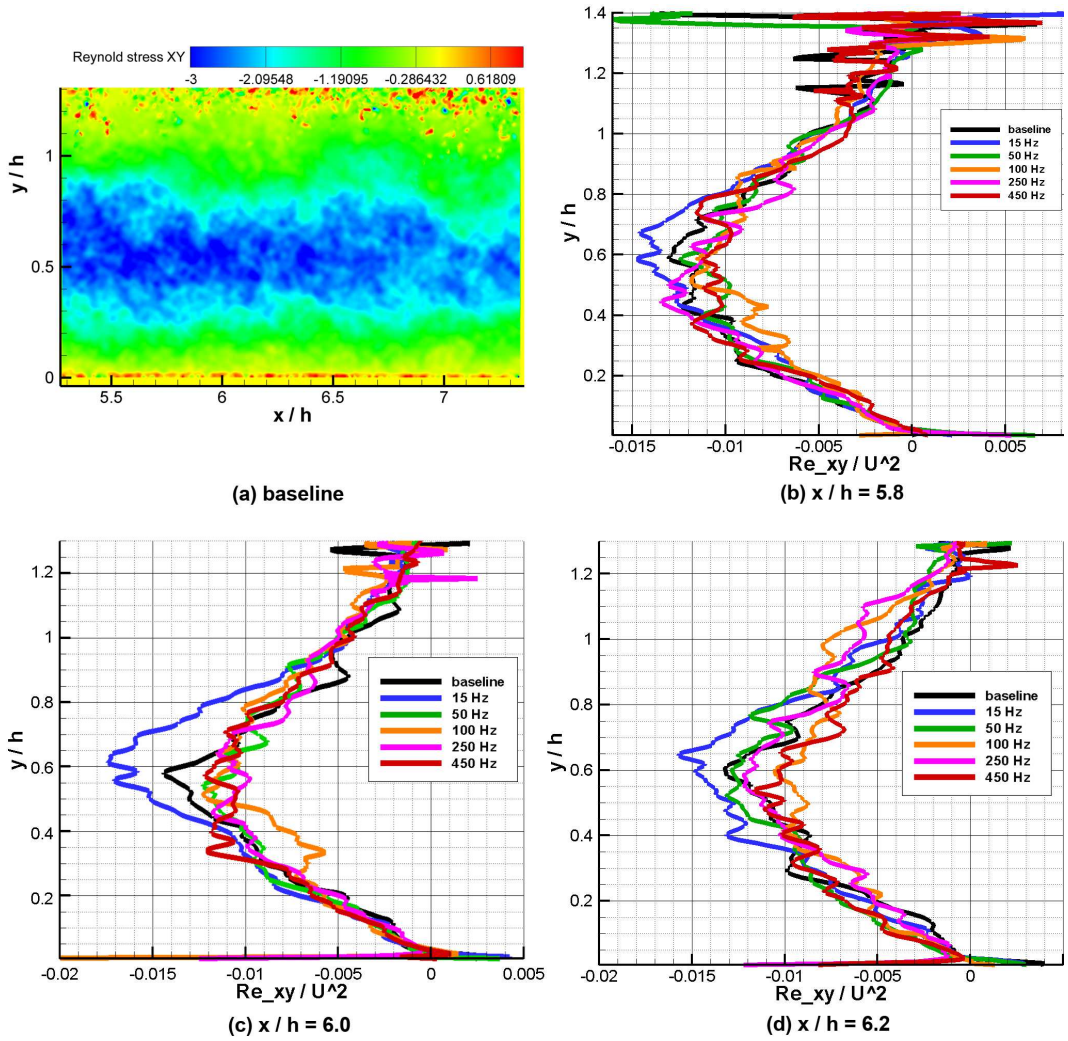

FIG. 15: Reattachment location: (a) Reynolds stress contours for baseline case; (b,c,d) effect of different frequencies on normalised Reynolds stress at three specific locations close to the reattachment point.

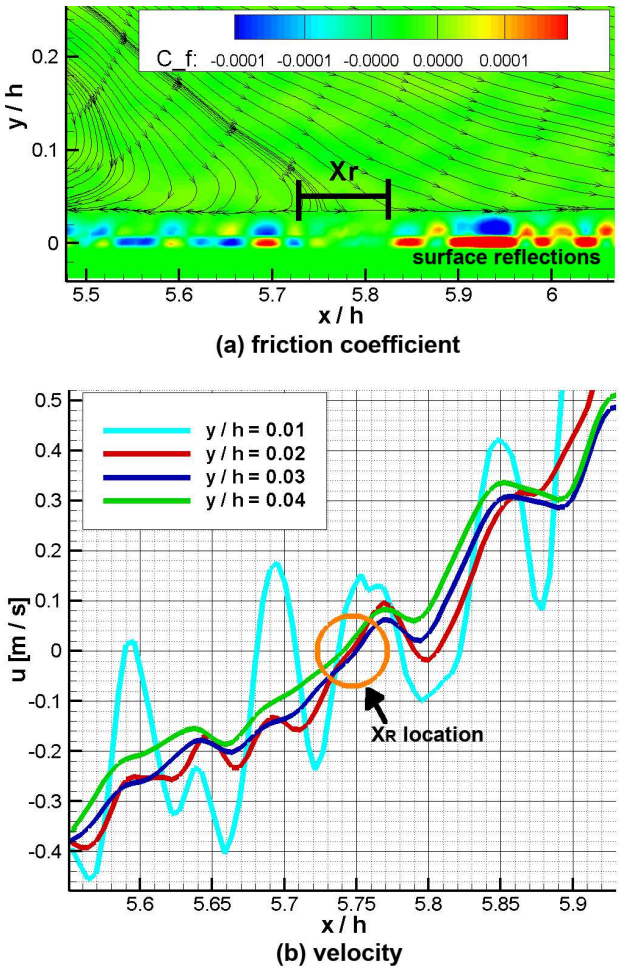

FIG. 16: Reattachment location for the baseline case: (a) the reattachment location is identified by the streamlines and the friction coefficient contours; (b) the stream-wise velocities (for $y/h = 0.02$, $y/h = 0.03$ and $y/h = 0.04$) reach zero at approximately $x/h = 5.75$ and show negative and positive values respectively before and after the reattachment point (the plot for $y/h = 0.01$ is disturbed by PIV errors on the floor surface).

ID	y/h	x/h	Mean [m/s]	Standard deviation	Standard error
P1	0.5	1	6.698	0.681	0.304
P2	1	1	7.099	0.376	0.168
P3	0.3	0.5	-0.308	0.234	0.104
P4	0.8	0.5	-0.176	0.696	0.311
P5	0.4	1.8	14.411	0.345	0.155
P6	0.5	1.5	13.688	0.323	0.144

TABLE I: Mean velocity, standard deviation and standard error of the velocity point samples used for the statistical accuracy check of PIV data.

	baseline	$15Hz$	$50Hz$	$100Hz$	$250Hz$	$450Hz$
x_R/h	5.75	5.80	5.81	5.94	5.84	5.70

TABLE II: Reattachment locations found for all the test cases.